

# Biodegradation by Cancer Cells of Magnetite Nanoflowers with and without Encapsulation in PS-*b*-PAA Block Copolymer Micelles

Emilia Benassai, Niéli Daffé, Elif Aygun, Audrey Geeverding, Emine Ulku Saritas, Claire Wilhelm, and Ali Abou-Hassan\*



Cite This: *ACS Appl. Mater. Interfaces* 2024, 16, 34772–34782



Read Online

ACCESS |



Metrics & More



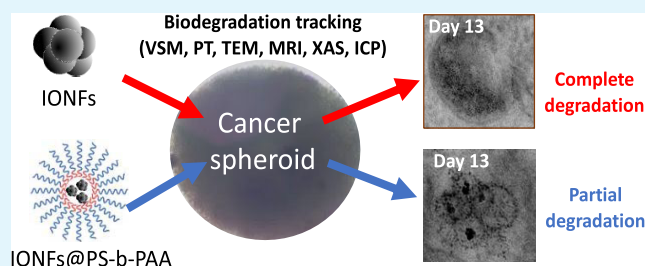
Article Recommendations



Supporting Information

**ABSTRACT:** Magnetomicelles were produced by the self-assembly of magnetite iron oxide nanoflowers and the amphiphilic poly(styrene)-*b*-poly(acrylic acid) block copolymer to deliver a multifunctional theranostic agent. Their bioprocessing by cancer cells was investigated in a three-dimensional spheroid model over a 13-day period and compared with nonencapsulated magnetic nanoflowers. A degradation process was identified and monitored at various scales, exploiting different physicochemical fingerprints. At a collective level, measurements were conducted using magnetic, photothermal, and magnetic resonance imaging techniques. At the nanoscale, transmission electron microscopy was employed to identify the morphological integrity of the structures, and X-ray absorption spectroscopy was used to analyze the degradation at the crystalline phase and chemical levels. All of these measurements converge to demonstrate that the encapsulation of magnetic nanoparticles in micelles effectively mitigates their degradation compared to individual nonencapsulated magnetic nanoflowers. This protective effect consequently resulted in better maintenance of their therapeutic photothermal potential. The structural degradation of magnetomicelles occurred through the formation of an oxidized iron phase in ferritin from the magnetic nanoparticles, leaving behind empty spherical polymeric ghost shells. These results underscore the significance of encapsulation of iron oxides in micelles in preserving nanomaterial integrity and regulating degradation, even under challenging physicochemical conditions within cancer cells.

**KEYWORDS:** magnetic nanoparticles, PS-*b*-PAA block copolymer, magnetic micelles, biodegradation, cancer cells spheroids



## 1. INTRODUCTION

Due to their multifunctional properties, iron oxide nanoparticles remain potent nanomaterials for the biomedical field. In addition, their biocompatibility makes them promising theranostics in this field. Thanks to their intrinsic magnetic properties, they can be manipulated and activated at a distance using magnetic fields,<sup>1–5</sup> enabling numerous applications such as imaging, triggered drug delivery, magnetic hyperthermia, magnetic targeting, and manipulation.<sup>6–10</sup>

Besides, in addition to their magnetism, magnetite iron oxides possess interesting optical features in therapeutic near-infrared (NIR) biological windows. When submitted to photostimulation, they can convert light to heat which can be used for biomedical photothermia (PT) such as in cancer therapy.<sup>6,11–13</sup> Polyol-synthesized magnetite iron oxide nanoflowers (IONFs) are to date among the best efficient magnetic nanoparticles for thermal therapies, with excellent photothermal performance in the therapeutic windows.<sup>12,14</sup> Their synthesis process and photothermal heating have been demonstrated and rationalized.<sup>14–18</sup>

Upon their interaction with cells and encapsulation in endosomes, nanoparticles can undergo structural modifications that can affect their properties and their ability to perform their

programmed tasks.<sup>19,20</sup> Understanding the impact of confinement and cellular bioprocessing on the structure, properties, and functions of nanomaterials in cells is crucial for designing efficient and sustainable nanomedicine. Three-dimensional (3D) cell spheroids offer a nice opportunity to study and track theranostics fate on different scales over time using diverse metrics.<sup>21</sup> They have provided valuable insights into the biodegradation of various nanomaterials, including optically active and magnetic ones.<sup>22–24</sup>

Recent reports on nanotheranostics have emphasized the role of the structure in modulating their biodegradation in solution, cells, or in vivo.<sup>19,25</sup> Different strategies have been explored including grafting of different types of ligands on their surfaces and encapsulation of the nanoparticles in organic shells such as imprinted porous polymers or inorganic silica shells.<sup>11,26–30</sup> Amphiphilic block copolymers (BCP) are a class

Received: May 28, 2024

Revised: June 20, 2024

Accepted: June 24, 2024

Published: June 29, 2024



of polymers that have attracted a lot of interest in materials science due to their versatility to self-assemble into different nanostructures as potential nanocarriers.<sup>31,32</sup> BCP can self-assemble with inorganic nanoparticles into hybrid nanoarchitectures of different functionalities while providing the inorganic part better stability, reduced toxicity, and protection from their environment.<sup>32–36</sup> Poly(styrene)-*block*-poly(acrylic acid) (PS-*b*-PAA) is one of the most extensively studied BCPs in the field of polymers. It has been explored for the coassembly of various types of nanoparticles including magnetic nanoflowers motivated by the versatility and rigidity of the micelles due to PS.<sup>36–39</sup> To overcome the limitations related to the large-scale production of magnetic micelles encountered in bulk, we have recently developed a high-throughput microfluidic strategy.<sup>39</sup> IONFs were encapsulated inside the polymeric PS and large-scale IONFs@PS-*b*-PAA magnetomicelles were produced. We showed that magnetomicelles are multifunctional theranostics with excellent photothermal functions when excited in the biosafe NIR–I–II window, in addition to being excellent  $T_2$  contrast agents in magnetic resonance imaging (MRI) and imaging agents for magnetic particle imaging.

Given the promising theranostic functions of the magnetic micelles in solution and the physicochemical properties of PS-*b*-PAA, it was evident to question whether the structural and functional integrities of the magnetomicelles are maintained once internalized in cells and consequently, if the PS core could serve as a relevant strategy to modulate the bioprocessing of the inorganic core in cancer cells.

In this study, we investigated the degradation of IONFs@PS-*b*-PAA magnetic micelles in a 3D spheroid cancer model. Employing a multiscale physicochemical and materials science approach, we traced the fate of magnetomicelles and nonencapsulated IONFs across different length scales using a plethora of tools. These include physical macroscopic metrics, such as magnetometry and photothermia, local metrics, such as transmission electron microscopy (TEM) for the morphology, and X-ray absorption spectroscopy (XAS) for analyzing the local chemical crystalline structure, supplemented by MRI. Overall, we demonstrate that the physicochemical conditions within cancer cells can overcome the plasticity of the PS core, leading to a mitigated degradation of the IONFs in the micelles. However, compared to nonencapsulated IONFs, the degradation in the magnetomicelles was slowed down. Besides, despite bioprocessing and biodegradation causing a loss of structural integrity of the polymeric PS core, the magnetic nanoparticles retained sufficient photothermal heating capability over a 13-day time scale.

## 2. MATERIALS AND METHODS

**2.1. Chemicals.** All of the products listed are of analytical purity grade, and they are used without further purification. Reagents and washing solvents are hydrochloric acid (HCl, 37%), nitric acid (HNO<sub>3</sub>, 68%), ammonia (NH<sub>3</sub>, 20%), ethanol (96%), acetone (>99%), diethyl ether (Et<sub>2</sub>O, 100%), and methanol (≥99.5%), all furnished by VWR International; trisodium citrate dihydrate (C<sub>6</sub>H<sub>5</sub>Na<sub>3</sub>O<sub>7</sub>·2H<sub>2</sub>O), oleic acid (>90%), and tetrahydrofuran anhydrous (THF, ≥99%) are supplied by Merck. The block copolymer polystyrene-*b*-poly(acrylic acid) (PS<sub>403</sub>-*b*-PAA<sub>62</sub>) is provided by Polymer Source, Inc. (Canada). Microfluidic material is supplied by Cluzeau info labo (C.I.L., France) and consists of a cross stainless-steel micromixer (10–32 for inner tubing 10/16", 0.040"), Teflon PFA tubing (10/16", 0.040"), and a PEEK tubing (360 μm × 150 μm, 0.006"). Calcein-AM (≥95.0%) is purchased from Merck,

while glutaraldehyde (25%) is purchased from Agar Scientific. Paraformaldehyde (16%), sodium cacodylate trihydrate, osmium tetroxide (OsO<sub>4</sub>, 4%), red ruthenium powder, and EPON resin are obtained from electron microscopy sciences (EMS). Oolong tea powder (O.T.E.) is purchased from Delta Microscopies (France), and agarose powder (low melting point) is obtained from Promega (France). Uranyl acetate powder is purchased from Prolabo.

**2.2. Synthesis of IONFs and Their Surface Modification.** The ferric (1.08 g, 4 mmol) and ferrous (0.39 g, 2 mmol) precursors were mixed in 80 mL of a mixture of DEG and NMDEA (1:1, v/v), under nitrogen atmosphere to prevent iron(II) oxidation, and dissolved overnight. In parallel, sodium hydroxide was dissolved in 40 mL of the same DEG/NMDEA mixture under nitrogen atmosphere; the alkaline solution was added to the iron precursor solution under magnetic stirring and nitrogen atmosphere 1 h before raising the temperature. Lastly, 500 μL of Milli-Q water was added to the reaction batch according to Hemery et al.<sup>18</sup> and the temperature was increased under reflux up to 220 °C. After cooling, the particles were magnetically separated and washed in HNO<sub>3</sub> (10%) to remove excess iron salts and confer to the NP surface a stabilizing positive charge, then twice with ethanol and acetone, before dispersing the final product in Milli-Q water. The surface of IONFs was modified by grafting citric acid to improve water solubility and oleic acid to obtain a stable ferrofluid in aprotic polar solvents. In brief, trisodium citric acid salts were dissolved in the aqueous ferrofluid, in a mole ratio  $n_{\text{C}_6\text{H}_5\text{Na}_3\text{O}_7}/n_{\text{NP}}^{\text{Fe}}$  equal to 0.13. The solution was heated to boil for 40 min, and after cooling, the product was washed three times with acetone and twice with ethyl ether, before being dispersed in Milli-Q water. Ammonia solution was added equimolarly to liquid oleic acid  $10 = n_{\text{OA}}/n_{\text{NP}}^{\text{Fe}}$  and magnetically stirred, in order to obtain a white thick mixture. At this point, also the IONF aqueous suspension was added and the solution was let to stir for 10 min at room temperature. Afterward, the temperature was raised to 50 °C for 30 min, and the product was separated from the solvent by magnetic separation. It was also washed three times with 60 mL of methanol, and after the last washing step, methanol was removed and a shiny precipitate was obtained; the final product was dispersed in tetrahydrofuran anhydrous. The oleate-coated IONFs were used for the microfluidic synthesis of magnetic micelles, while citrated NFs were used as a control in all experiments.

**2.3. Microfluidic High-Throughput Synthesis and Scaling Up of Magnetomicelles.** Magnetomicelles were formed by nanoprecipitation: two solutions of PS-*b*-PAA ( $M_n = 41,000$ – $4200$ , 1.8 g/L) and oleic acid-coated IONFs (0.2 g/L) were mixed in a ratio of 4:1 v/v to prepare a stock solution that was ultrasonicated for some minutes before use. Three ECP2000 Analytical HPLC pumps (ECOM spol. s r.o., Czech Republic) were connected to a stainless-steel cross junction: one central inlet was connected to the 150 μm PEEK tube, and it was used for injecting the solution of block copolymer and NFs in THF; two symmetrical inlets were used to pump Milli-Q water. The outlet consisted of a flow-focusing system with water surrounding a THF-focalized stream. Water and THF were pumped into the system in a 7:1 v/v ratio ( $\alpha$ ) at variable total flow rates ( $Q_{\text{tot}} = 0.4$ – $22.8$  mL/min). All syntheses were conducted in triplicate to assess reproducibility. After synthesis, a mass of Milli-Q water equal to half of the total mass of the fluid mixture was rapidly added to quench the growth of micelles and preserve the obtained conformation. The resulting solution was collected in a pear-shaped flask to eliminate THF through rotary evaporation (BUCHI rotavapor R-210, connected to a BUCHI vacuum pump V-700 and employing a BUCHI heating bath B-491). The micellar water suspension was filtered with a 0.45 μm Minisart filter unit (Sartorius, Gottingen, Germany); it was let to precipitate on a permanent magnet, and the pellet was collected and washed thrice with Milli-Q water and subsequently stored at 4 °C.

**2.4. Nanostructure's Characterizations.** The morphology of the NPs was imaged using a JEOL-1011 transmission electron microscope operating at 100 kV. Size distributions were determined using the open-source ImageJ software, manually measuring 300 NPs on at least three different images. The resulting histograms were modeled by a log-normal law using Igor Pro 7 software to determine

the mean physical diameter ( $d_{\text{TEM}}$ ) and the polydispersity ( $\sigma_{\text{TEM}}$ ) of each sample. The total iron concentrations of the NPs suspensions were measured by atomic absorption spectroscopy (AAS, PinAAcle 500, PerkinElmer) by degrading the samples in concentrated HCl (37%) before a dilution in  $\text{HNO}_3$  (2%). Ultraviolet–visible–NIR (UV–vis–NIR) spectra (400–1100 nm) were recorded at room temperature in a 1 cm quartz cuvette using an Avantes spectrophotometric setup composed of an AvaLight-DHc lamp connected by optical fibers to a StarLine AvaSpec UV/vis detector and to an NIRLine AvaSpec-NIR256–1.7 NIR detector. Aqueous suspensions were measured by VSM analysis in a static magnetic field comprised between  $-1$  and  $1$  T at 300 K. Infrared PT experiments were carried out using a 0.5 mL Eppendorf containing 50  $\mu\text{L}$  of the NP suspensions excited for 300 s by an NIR laser (1064 nm, 0.28 W/ $\text{cm}^2$ ) coupled to an optical fiber from Laser Components SAS (temperature increase is measured by an infrared camera FLIR SC7000).

### 3. SPHEROIDS

**3.1. Spheroids Formation.** U87 MG human glioblastoma cells were selected for cancer cell line model and purchased from ATCC. They were cultured in Dulbecco's modified Eagle's medium (DMEM, Gibco), supplemented with 1% penicillin-streptomycin (PS, Gibco) and 10% fetal bovine serum (FBS, Gibco), within a 37 °C humidified incubator with 5%  $\text{CO}_2$ . Flasks of U87 cells were incubated at 37 °C and 5%  $\text{CO}_2$  overnight with NP-doped complete culture medium (DMEM containing PS and FBS). IONF NPs were incubated at a dose of 0.05 mM, while IONF@PS-*b*-PAA NPs were incubated at a dose of 0.5 mM. After the incubation, the cells were left an additional hour in the incubator at 37 °C to allow the complete internalization of the nanoparticles adsorbed at the external membrane of cells; successively, the cells were rinsed with complete medium, detached, and counted. Cellular pellet was formed by centrifugation and subsequently dispersed in an appropriate amount of fresh culture medium. The resulting volume was then separated in 0.5 mL Eppendorf (each containing 200 000 cells), centrifuged at 180xg, and incubated at 37 °C to allow cell-to-cell adhesion and the formation of the spheroids.

**3.2. Spheroids Characterization.** **3.2.1. Vibrating Sample Magnetometry (VSM).** Spheroids were fixed on different maturation days. They were washed with PBS and placed in a paraformaldehyde solution (PFA, 4% in PBS) for 2 h at room temperature. Afterward, the fixative solution was removed and spheroids were washed twice with PBS and stored at 4 °C before characterizations. Magnetometry analyses were conducted on 10 spheroids samples ( $n = 10$ ) for each maturation time using a Quantum Design PPMS at 300 K between 0 and 2 T, or between  $-0.15$  and  $0.15$  T.

**3.2.2. Iron Concentration Determination.** Iron concentrations were obtained by induced-coupled plasma atomic emission spectroscopy (ICP-AES, iCAP 6500, Thermo) after degradation of 10 spheroids ( $n = 10$ ) for each maturation time in concentrated  $\text{HNO}_3$  (68%) before dilution in water (up to 2%).

**3.2.3. Transmission Electron Microscopy.** Prior to their observation, spheroids ( $n = 5$ ) were fixed at different maturation days for inclusion. They were washed five times in cacodylate buffer (0.1 mol·L) for 10 min under orbiting agitation. They were contrasted with oolong tea extract (OTE, 0.2%) in cacodylate buffer (0.1 mol·L) and newly washed according to the previously described procedure. Samples were then postfixed with a solution in cacodylate buffer (0.1 mol·L)

of osmium tetroxide ( $\text{OsO}_4$ , 1%) and potassium ferrocyanide (KFC, 1.5%), on ice and sheltered from light. Samples were washed in ultrapure water and successively enrobed in agarose (4% in ultrapure water). Samples are then dehydrated with successive baths of ethanol (once at 50%, once at 70%, once at 95%, once at 100%, and five times at 100% absolute ethanol, purchased from VWR) for 15 min on ice. Impregnation with epoxy resin (Epon) was obtained through subsequent baths under rotary agitation in absolute ethanol/resin mixtures (1:2 v/v for 1 h, 1:3 v/v overnight, and 1:4 for 1.5 h), in pure resin (two baths of 3 h and overnight), and in pure resin with benzyldimethylamine (BDMA) polymerization accelerator (two baths of 3 h after degassing the samples under vacuum for 30 min). Then, a bed of resin with BDMA was poured into molds and polymerized at 60 °C for 1 h, before positioning the samples, covering them with resin, and storing them in the preheated stove at 60 °C for polymerization (lasting 72 h). Ultrathin sample slices of 100 nm were obtained with a UCT ultramicrotome (Leica). Sample cuts were collected and placed on carbon-coated copper grids 200 mesh; then, the contrast was reinforced after staining with a solution of uranyl acetate (2.5% in water, 15 min sheltered from light). The morphology of the internalized NPs in cells was imaged using alternatively a JEOL-1011 transmission electron microscope operating at 100 kV, equipped with a charge-coupling derived camera (Orius) or a JEM-2100 transmission electron microscope (JEOL) operating at 80 kV with a LaB6 filament and equipped with a 2k × 2k Veleta charge-coupling camera (Olympus Soft Imaging Solutions).

### 4. DETERMINATION OF DEGRADATION % USING VSM IN THE SPHEROIDS

First, aqueous suspensions of IONFs and IONFs@PS-*b*-PAA were measured by VSM analysis in a static magnetic field comprised between  $-1$  and  $1$  T at 300 K, to retrieve the value of saturation magnetization ( $M_s$ ) with  $M_s = \frac{M_{\text{max}}}{m_{\text{NPs}}}$ .  $M_{\text{max}}$  is the maximum saturation of the IONFs after reaching magnetic saturation (expressed in emu), and  $m_{\text{NPs}}$  is the mass of IONFs in the suspension, obtained from  $m_{\text{NPs}} = \frac{V_{\text{tot}} \cdot \phi \cdot \rho_{\text{Fe}_3\text{O}_4}}{100}$ , where  $V_{\text{tot}}$  is the total volume of the suspension,  $\phi$  is the volume fraction of IONFs in the suspension, and  $\rho$  is the density of magnetite ( $\rho = 5.2$  g/ $\text{cm}^3$ ). The average mass of magnetic NPs per spheroid derived from VSM ( $m_{\text{day},i}$ ) for each day  $i$  ( $i = 1, 3, 7, \text{ and } 14$ ) was next calculated. The percentage of degradation of the NPs is calculated then by (%) =  $\frac{m_{\text{day},i} - m_{\text{day},i,\text{ICP}}}{m_{\text{day},i,\text{ICP}}} \times 100$ , where  $m_{\text{day},i,\text{ICP}}$  corresponds to the average mass of total iron per spheroid deduced by ICP-AES analysis for each maturation day  $i$ .

### 5. MAGNETIC RESONANCE IMAGING (MRI) EXPERIMENTS

To investigate the effects of degradation on the MRI signal of the IONFs and IONFs@PS-*b*-PAA in spheroids, their  $T_2$  relaxation time constants were measured on a 3 T MRI scanner (Siemens Magnetom Trio) using a 32-channel head coil. Samples contained spheroids treated with IONFs or with IONFs@PS-*b*-PAA. For each type, 4 samples ( $n = 4$ ) were prepared with different spheroid maturation days (1, 3, 7, and 10 days). To ensure careful measurement of  $T_2$  relaxation times, the samples were submerged into a gel prepared with

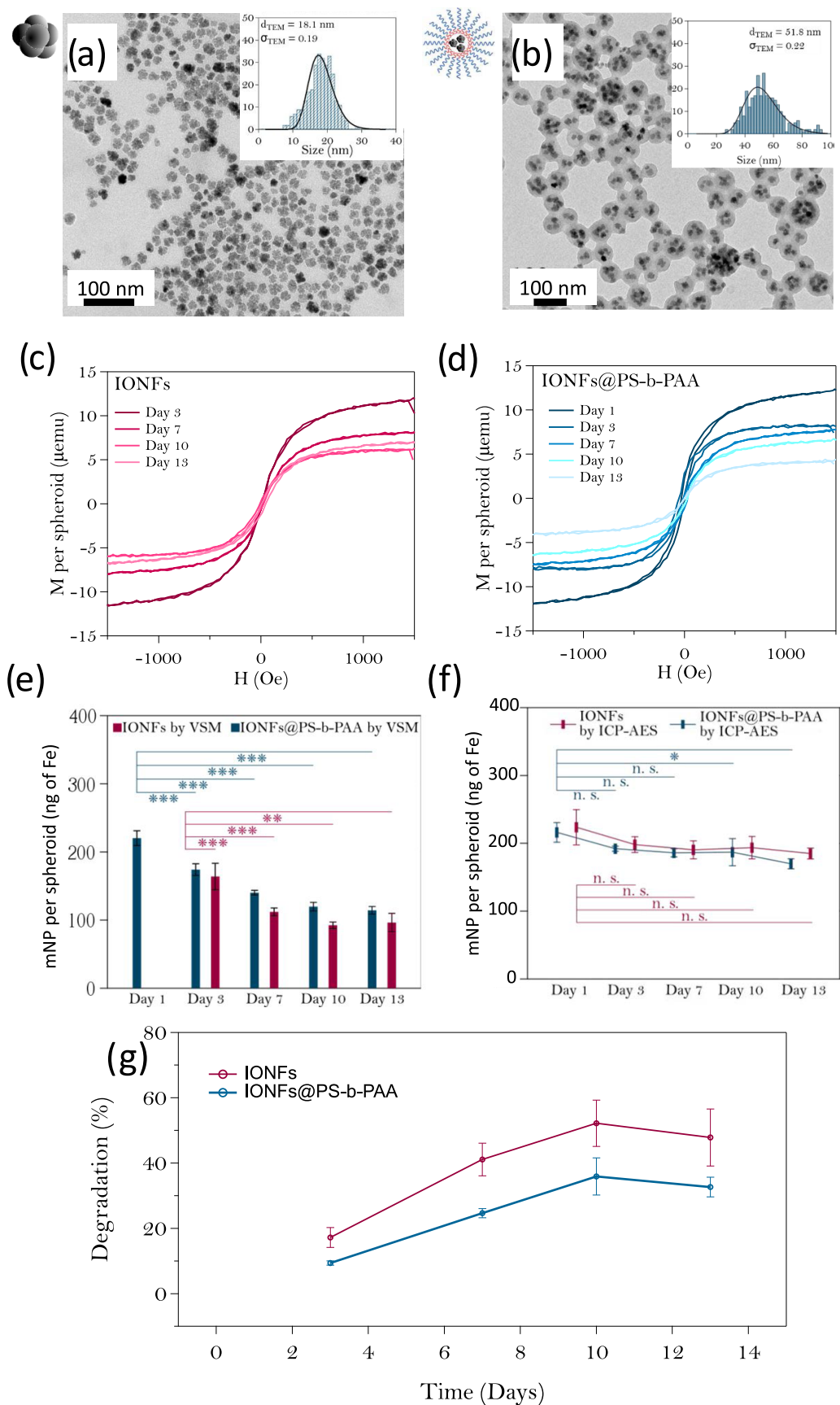


**Figure 1.** TEM image and size distribution histogram fitted by a log-normal law for IONFs (a) and IONFs@PS-*b*-PAA magnetomicelles (b). Magnetization per spheroid measured after internalization in U87 cancer cells and maturation of a spheroid model ( $n = 10$ ) for 1, 3, 7, 10, and 13 days for IONFs (c) and IONFs@PS-*b*-PAA (d). Residual magnetic iron per spheroid expressed in ng measured by VSM for each maturation day ( $n = 10$ ) for both IONFs and IONFs@PS-*b*-PAA (e). Black bars stand for standard deviations. A two-tailed Student's *t* test was used to assess the

Figure 1. continued

significance of residual magnetic iron for both samples on the same day (black trait and stars) and for same IONFs after 3, 7, 10, or 13 days of maturation (burgundy trait and stars for IONFs, blue trait and stars for IONFs@PS-*b*-PAA).  $0.05 > p\text{-value} > 0.01$  (\*),  $0.01 > p\text{-value} > 0.001$  (\*\*),  $p\text{-value} < 0.001$  (\*\*\*)). (f) Total iron per spheroid (expressed in ng,  $n = 10$ ), measured by ICP-AES. Colored bars stand for standard deviations. A two-tailed Student's *t* test was used to assess the significance of residual magnetic iron for the same IONFs after 3, 7, 10, or 13 days of maturation.  $0.05 > p\text{-value} > 0.01$  (\*),  $0.01 > p\text{-value} > 0.001$  (\*\*),  $p\text{-value} < 0.001$  (\*\*\*)). (g) Percentage of NPs degradation deduced from VSM measurements for IONFs and IONFs@PS-*b*-PAA.

HEC and doped with  $\text{Cu}_2\text{SO}_4$  to ensure the MRI signal of the environment around the spheroids was at a reasonable level, similar to human tissue signal. For measuring  $T_2$ , a single-echo spin echo sequence was utilized.  $T_2$ -weighted images were acquired at 16 different echo times (TE) ranging between 8.5 and 1000 ms, with TR = 2000 ms. A field of view (FOV) of  $12 \times 12 \text{ cm}^2$  with 4 mm slice thickness was imaged, using a  $128 \times 102$  acquisition matrix. Images were analyzed using an in-house MATLAB (Mathworks) script. A fixed-size region of interest (ROI) was placed over the image region corresponding to each vial. The  $T_2$  value for each sample at each pixel in the ROI was determined using the following monoexponential decay equation:  $S = S_0 e^{-TE/T_2}$ .

## 6. X-RAY ABSORPTION MEASUREMENTS (XAS)

The X-ray data were acquired at the X-Treme beamline (Swiss Light Source, Paul Scherrer Institut). X-ray absorption measurements were performed on a collection of three spheroids ( $n = 3$ ) deposited on Si wafers for each maturation time. XAS at the Fe  $L_{2,3}$  edges (700–730 eV) were collected at 300 K using the total electron yield mode of detection. The spectra were normalized by the edge jump at the maximum of  $L_3$  after background subtraction.

## 7. RESULTS AND DISCUSSION

**7.1. Encapsulation of IONFs in the Micelles Decreases Their Degradation as Shown from VSM.** Figure 1a,b shows TEM images of the magnetite IONFs before and after encapsulation in the polymeric micelles. As displayed from the size histograms (insets) fitted by a log-normal law, the IONFs have a diameter of 18.1 nm with a polydispersity of 0.19, as calculated from the size distribution histogram, while the magnetic micelles are 51.8 nm in size with a polydispersity of 0.22. The IONFs were synthesized through the polyol process and the magnetic micelles were produced by self-assembly of the IONFs and the BCP using a high-throughput microfluidic method, as described recently.<sup>39</sup> The magnetization curves for the colloidal aqueous suspensions of IONFs and magnetomicelles are shown in Figure S1. The citrated IONFs exhibited a saturation magnetization ( $M_s$ ) of 79  $\text{emu/g}_{\text{NPs}}$ , consistent with previously reported values for magnetite IONFs.<sup>17</sup> However, the magnetomicelles showed a lower  $M_s$  value of 61  $\text{emu/g}_{\text{NPs}}$ , attributed to the presence of the polymeric material, as reported for iron oxides embedded in some matrices.<sup>40,41</sup>

To investigate the impact of cancer cell processing on both types of nanostructures, a spheroid-forming human glioblastoma cell line (U87) was used as a cancer model. Cancer cells were incubated with both types of nanostructures to allow for their uptake by the cells at a biocompatible concentration and a final concentration (see Section 2).<sup>39</sup> Due to their excellent stability, the micelles penetrate cells less readily compared to nonencapsulated bare IONFs, justifying a higher dose incubation for the micelles to achieve the same amount of

cellular magnetism postinternalization. Following this, spheroids containing approximately 200,000 cells were formed and allowed to mature for up to 13 days at 37 °C. The spheroids were fixed at different maturation days (1, 3, 7, 10, and 13 days, Figure S2). After internalization of the NPs in the cancer cells and the formation of the spheroids, we followed and quantified their degradation in the cancer spheroids with days at the nanoscale using their magnetic fingerprints by vibrating the sample magnetometry (VSM).

As shown in Figure 1c,d, the magnetization of IONFs and IONFs@PS-*b*-PAA decreased progressively over maturation times, indicating degradation of the iron oxide core. The average mass of IONFs per spheroid was then calculated from the VSM measurements. The results showed that the mass of magnetic material per spheroid for both IONFs and magnetomicelles decreased with spheroid maturation time. Statistical analysis revealed significant differences in the mass of magnetic material between day 1 and other maturation days for most conditions. Such differences decreased with maturation time, becoming nonsignificant at day 3, and remaining nonsignificant at days 7, 10, and 13. ICP-AES measurements were performed to determine the average total iron concentration within single spheroids. Total iron per spheroid was perfectly similar for spheroids incubated with IONFs or with magnetomicelles. Besides, these values remained relatively stable over the whole maturation period, with yet a decreasing tendency in the amount of total iron per spheroid over the maturation period. To assess whether the decrease in total iron was due to cellular loss, the two-tailed Student's *t* test was performed on sets of total iron values obtained for single spheroids at maturation day one against all other maturation days. Except for the spheroids with magnetomicelles at maturation day 13, which showed a significant difference, all other conditions did not exhibit significant differences, indicating minimal cellular loss. The percentage of degradation was calculated by considering the mass of magnetic material extracted from VSM and the average value of iron obtained by ICP-AES as detailed in Section 2. Results (Figure 1g) showed a general increase in the degradation percentage with the maturation time for IONFs and magnetic micelles. However, the degradation of IONFs was faster than that of magnetic micelles reaching at day 13 a value of 48 ( $\pm 9$ )% for IONFs and 33 ( $\pm 3$ )% for IONFs@PS-*b*-PAA. These results suggest that the polymeric micelles can provide a protective behavior after internalization in U87 cells.

**7.2. Photothermal Function of IONFs Lasted Longer When Encapsulated in the Micelles.** The UV–vis–NIR extinction spectra of IONFs and the magnetomicelles are shown in Figure S3. Both spectra show a U-shaped absorption and an increase above 700 nm, characteristic of magnetite and its intervalence charge transfer band. However, the spectrum of the magnetomicelles displayed a slight decrease in the absorbance compared to the nonencapsulated IONFs, which was attributed to the presence of the polymeric shell, with no significant impact on the heating efficacy of the encapsulated

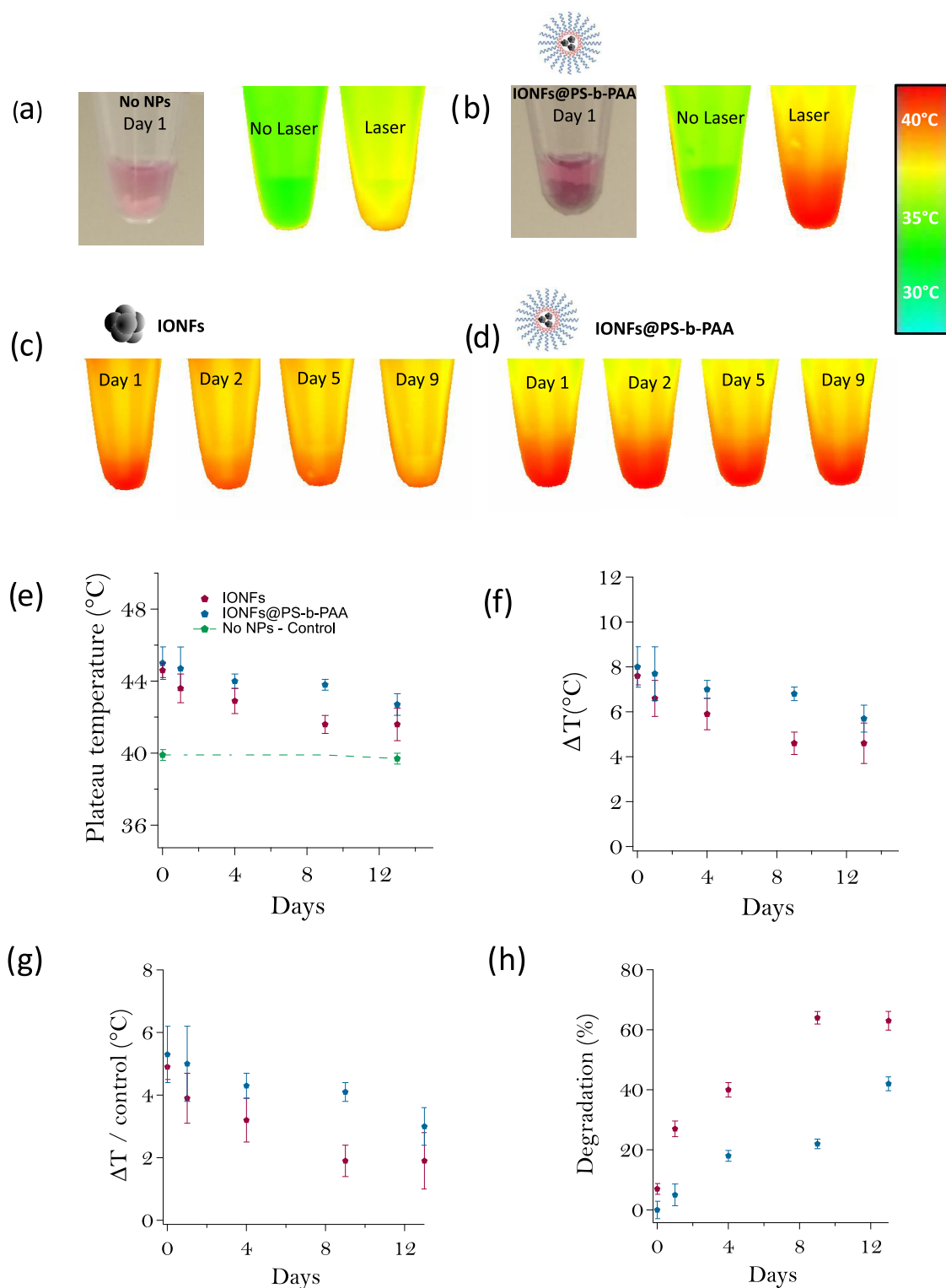


**Figure 2.** After the formation of the spheroids, they are individually collected in 0.5 mL Eppendorf tubes, with a quantity of 24 spheroids per tube in 25  $\mu\text{L}$ . For the condition shown in (a), the spheroids are control spheroids, which have not been in contact with nanoparticles. They appear relatively white and exhibit minimal heating under an IR laser at 1  $\text{W}/\text{cm}^2$  (images captured by the IR camera shown on the right before and after laser application, over a duration of 10 min). (b) The same data but for spheroids fabricated from cells that have internalized magnetic micelles. Heating is more significant, reaching about 46  $^{\circ}\text{C}$  over 10 min of laser exposure. (c, d) Heating of  $n = 24$  spheroids in a 0.5 mL Eppendorf tube filled with 25  $\mu\text{L}$ , but this time not only on day 0 (as in panels (a, b)) but also on days 1, 4, and 9. In (c), the spheroids were formed from cells that internalized the nanoflowers, while in (d), it was cells that internalized the magnetic micelles. For each time point, measurements were performed on 4 sets of  $n = 24$  independent spheroids. The average plateau temperature reached is shown in (e), and the temperature increase is shown in (f), and normalized to the control in (g). Finally, the percentage of degradation is calculated and shown in (h).

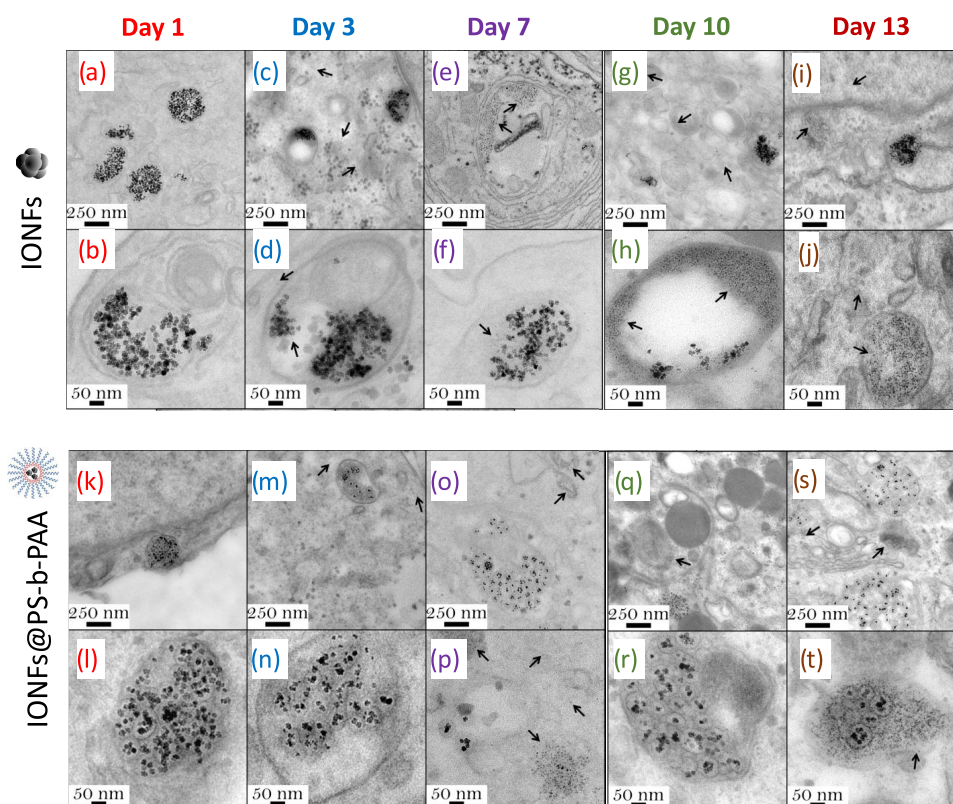


**Figure 3.** Representative TEM micrographs of IONFs (a–j) and IONFs@PS-*b*-PAA (k–t) NPs after internalization in U87 cells for different days: 1-day-long (a, b, k, l), 3-day-long (c, d, m, n), 7-day-long (e, f, o, p), 10-day-long (g, h, q, r), and 13-day-long (i, j, s, t) maturation into spheroid models. Black arrows indicate ferritin-enriched areas. More images are provided in Figures S5 and S6.

IONFs when irradiated in the NIR, as it was demonstrated in a previous work.<sup>39</sup> In order to assess the effect of intracellular degradation of nanomaterials on photothermal activity, we implemented a measurement protocol on spheroids under irradiation with an 808 nm laser at a power density of 1 W/cm<sup>2</sup>. Under these conditions, the temperature elevation at the single spheroid level is not detectable compared to nonspecific heating. Consequently, we systematically gathered 24 spheroids in a 0.5 mL Eppendorf tube containing 25  $\mu$ L of culture medium (typical photograph of those multiple spheroids can be observed in Figure 2a,b). Figure 2a,b also depicts the heating in an image captured by an infrared camera for 24 control spheroids (nonspecific heating) and for 24 spheroids composed of cells that have internalized magnetic micelles. Figure 2c,d displays representative images of heating for the two types of nanomaterials, particularly at different stages of spheroid maturation, namely, days 0, 1, 4, and 9. Each measurement was conducted on 4 independent samples, each containing 24 spheroids, for every time point, totaling 100 spheroids per data point (days 0,1,4,9, and 13), and thus approximately 500 spheroids in total. Figure S4 shows the temperature elevation curves for each sample, and Figure 2e–g shows the average plateau temperatures achieved after 10 min of laser exposure, the equivalent temperature elevation, and the temperature elevation excluding the contribution of nonspecific heating, respectively. This clearly identifies protection provided by the micelles against degradation, as quantified in Figure 2h, resulting in a longer-lasting photothermal potential for them.

### 7.3. Nanoscale Observations by Electron Microscopy Evidence That Cancer Cells Can Overcome the

**Polymeric PS Core Barrier and Induce Slight Biodegradation of IONFs.** We next tracked at the nanoscale the morphological features of IONFs including in the micelles when processed by cancer cells. For this, slices of the fixed spheroids were imaged at different days using TEM. Representative microtomy images of the U87 spheroids formed with cells containing either IONFs or magnetomicelles are shown in Figure 3. For spheroids fixed at day 1 of maturation, no significant changes were observed between the size distributions of the IONFs in suspension and in the cells. In addition, they were initially found in membrane-enclosed compartments of the cytosol, mainly identifiable as early endosomes (Figure 3a). Higher-magnification micrographs of the same IONFs on day 1 (Figure 3b) also reveal IONFs enclosed in larger vesicles, resembling double-layered autolysosome, associated with autophagy-related acidic degradation pathways.<sup>42</sup> This result aligns with cancer cell-enhanced metabolism and autophagy, to escape apoptotic programmed cell death and promote cell survival in the case of metabolic stress. Autophagy is also related to cancer cells' ability to develop resistance to external stressors, including chemotherapeutic drugs and nanoparticles.

Micrographs on day 3 of spheroid maturation showed the colocalization of IONFs in gray-contrasted organelles, probably derived from the fusion of endosomes with lysosomes (Figure 3c,d). Iron-loaded ferritin, indicated by black arrows, was also observed in these structures, suggesting that the endocytic compartments underwent acidification, leading to the appearance of iron-loaded ferritin. From maturation days 7, 10, and 13 (Figure 3e–j) low-contrast 4–7 nm spheres consistent with iron-charged ferritin were found within

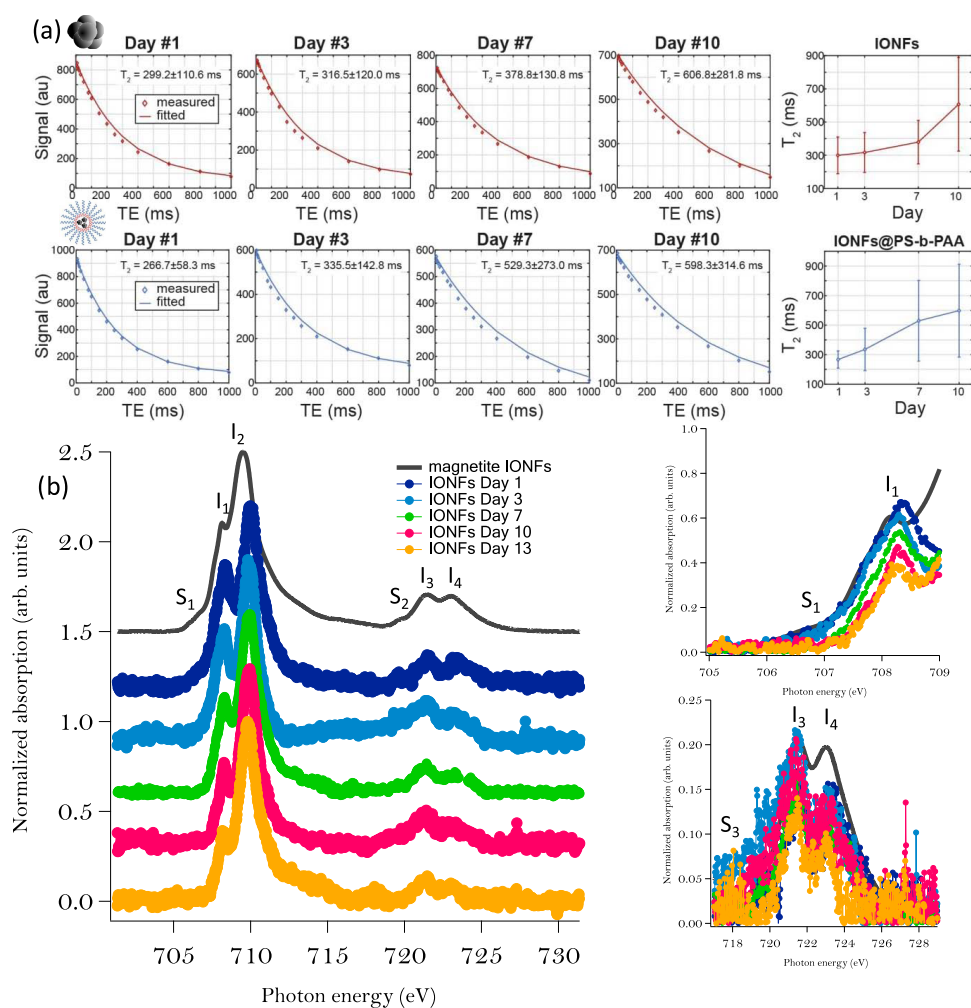


**Figure 4.** (a) MRI  $T_2$  relaxation times for different maturation days for IONFs and IONFs@PS-*b*-PAA and as a function of days with increased  $T_2$  indicating degradation of the nanoparticles ( $n = 4$ ). Error bars denote standard deviations. (b) XAS at the Fe  $L_{2,3}$  edges performed on the IONFs spheroids ( $n = 3$ ) for maturation times of 1, 3, 7, 10, and 13 days. The results can be compared with the XAS acquired on the magnetite reference nanoparticles as synthesized (before internalization). The insets show the normalized XAS data for comparison in the  $L_3$  edge (top) and  $L_2$  edge (bottom).

multimembrane amphisomes or auto- and endolysosomes. In contrast, very few intact IONFs were detected on the grid in the same vesicles. However, some endosomes containing only intact IONFs were also present, confirming that degradation occurred sporadically at the level of single vesicles.

Regarding the spheroids incubated with magnetomicelles, the nanostructures were mainly localized in early endosomes (Figure 3k,l) or autophagosomes (displaying portions of double-layered membranes, as shown in Figure 3m,n up to 3 days after incubation with cells). Notably, not all IONFs appeared to be encircled by the polymeric shell; some seemed to have been freed in the endosomal lumen. Starting from the third day of spheroid maturation, the presence of iron-loaded ferritin (Figure 3n) indicated the degradation of IONFs, likely through the same acidic pathway observed for IONFs. The ferritin-like spheres were found in both membrane-enclosed dark-gray compartments and in the cytosol at maturation day 7 (Figure 3o,p), suggesting lysosomal engagement. This was further confirmed by micrographs obtained at maturation day 10 (Figure 3q,r), showing autophagolysosomes and endolysosomes. Even after 13 days of magnetomicelles internalization in U87 cells, ferritin-enriched areas were still identifiable in dark-

gray endosomes and free in the cytoplasm, next to intact IONF@PS-*b*-PAA NPs (Figure 3s,t). Interestingly, one micrograph (Figure 3t) showed the coexistence of iron-loaded ferritin, intact magnetomicelles, and empty nondenatured polymeric “ghost” shells (where ferritin appeared to stick onto the polymeric surface). This observation confirmed the escape of IONFs through degradation from the still intact polymeric shell rather than the disruption or degradation of the polymer itself. The size of the intact shells did not show any significant change in size compared to that of the initial suspension of magnetic micelles.

#### 7.4. MRI and XAS Investigations Confirmed the Biodegradation of IONFs and the Formation of Ferritin.

IONFs were recently described as excellent  $T_2$  contrast agents for MRI.<sup>39</sup> Here, we used  $T_2$ -weighted MRI after internalization in the spheroids to monitor their degradation with time. Figure S7 illustrates an example  $T_2$ -weighted MRI image depicting eight spheroid samples within the gel environment. Figure 4a shows how  $T_2$  changes for IONFs and magnetomicelles on days 1, 3, 7, and 10 with maturation time. Lower  $T_2$  values indicate better MRI contrast performance. Notably, the  $T_2$  values for both IONFs and magnetomicelles increase

with time, suggesting a gradual loss of the MRI contrast performance due to degradation. Statistical analysis via a two-tailed Student's *t* test revealed significant differences in  $T_2$  values between day 1 and day 10 for both IONFs and magnetomicelles. This behavior can be attributed to degradation-induced reduction in the effective concentration of magnetic nanoparticles within the spheroids for both cases.<sup>43</sup>

Additionally, Figure 4a shows that both IONFs and magnetomicelles display comparable  $T_2$  values on day 10. Taken together, TEM images and MRI demonstrate that cancer cells can bioprocess the magnetic nanoparticles leading to their degradation, which correlates well with the decrease in their magnetic properties observed by VSM and photothermal measurements. These results also demonstrate that, despite their encapsulation inside a polymeric barrier of PS with high glass transition, chemical species in the cancer cell can still access the magnetic nanoparticles inducing their degradation. Indeed, Vyhňalkova et al.<sup>38</sup> have shown that small species are capable of diffusing in empty PS-*b*-PAA polymeric micelles leading to a decrease in the glass transition temperature of the BCP, an increase in the mobility of PS chains, enabling access of species to the core of the micelle. In addition, an acidic pH as encountered in the endosomal compartments of cancer cells may affect the conformational behavior of the hydrophilic PAA corona or even lead to its degradation.<sup>27,44</sup> Taking together these elements, we may draw the following hypothesis in the cancer cells where the harsh physicochemical conditions (pH, ROS, etc.) and high metabolism can lead to the formation of different species capable of diffusing into the core of the micelles leading to the degradation of IONFs through their dissolution into iron species.

To further investigate the chemical and structural changes in the IONFs during their degradation, we examined X-ray absorption spectroscopy (XAS) at the Fe  $L_{2,3}$  edges for various maturation time points, as shown in Figure 4b. Before internalization in spheroids the citrated magnetite IONFs used as a reference, we presented a typical  $L_{2,3}$  edges resonance spectrum with a prominent feature at 709.5 eV ( $I_2$ ) and a lower-intensity peak at 708 eV ( $I_1$ ) at the  $L_3$  edge, and two smaller features at 721.5 eV ( $I_3$ ) and 723 eV ( $I_4$ ) for the  $L_2$  edge.<sup>45–47</sup> In addition, small shoulders at lower energies  $\sim$ 706.3 and  $\sim$ 719 eV of the  $L_3$  and  $L_2$  edges, respectively, revealed the clear presence of octahedral coordinated  $Fe^{2+}$ . Qualitatively, the contribution of octahedral  $Fe^{2+}$  is not as strong as expected for a stoichiometric bulk magnetite revealing that the magnetite particles are slightly oxidized.<sup>48,49</sup> Right after internalization (day 1) and compared with the IONFs in water, a more pronounced splitting of the  $L_3$  edge and increased prominence of I1 was observed. This was accompanied by a higher ratio in the intensity of  $I_3/I_4$ . Taking into account that no degradation was spotted at day 1 by VSM, PT, and TEM measurements, this observation may be explained by the presence of a native  $Fe^{2+}$  pool in the spheroids, which contributes in addition to magnetite IONFs to the final XAS signal. Furthermore, with spheroids maturation days we noticed additional evolutions of the isotropic signal contributions. From day 1 to day 13, this peak at the  $L_2$  edge experienced a clear decay with the maturation time of the spheroids. Simultaneously, the  $I_3/I_4$  ratio gradually increased from day 1 to day 3, while S1 and S2 contributions decreased, disappearing by day 13. These results indicate a process of oxidation of the ferrous species, which can occur

through transformation into another phase of IONFs. The shape of the XAS spectra indicates that as the spheroids mature, they contain Fe atoms in an environment characteristic of ferrihydrite.<sup>50,51</sup> These results agree well with the images obtained at the nanoscale by TEM showing the degradation of IONFs and the formation of ferritin. Precise crystalline phases of the nanoparticles during maturation may be sensitive to XAS features due to the possible mixing of different iron oxide phases, but this is beyond the scope of our current study. Nevertheless, we can confidently conclude that IONFs evolve into a more oxidized ferrihydrite phase with maturation time.

## 8. CONCLUSIONS

In this paper, we investigated the bioprocessing of IONFs and magnetic micelles made by self-assembly of IONFs and PS-*b*-PAA block copolymer in U87 glioblastoma cancer spheroids. Using different characterization tools, we monitored the biotransformation of the assembled structures and non-encapsulated IONFs at different times and length scales. We showed that while the polymeric barrier around the magnetic nanoparticles is kept intact, it can be overcome by the harsh physicochemical conditions of the cancer cells inducing partially the degradation of the magnetic nanoparticles in the core of the micelles and the formation of ferritin. Yet, degradation is less pronounced for the magnetomicelles than for the nonencapsulated IONFs. On the therapeutic side, this protection translates into a longer-lasting photothermal performance of the magnetomicelles. These results therefore underlie the potential of micelles as nanocarriers and protection agents for inorganic nanoparticles and may open new perspectives for the development of innovative therapies in the field of nanomedicine, such as in drug delivery or tissue engineering.

## ■ ASSOCIATED CONTENT

### Supporting Information

The Supporting Information is available free of charge at <https://pubs.acs.org/doi/10.1021/acsami.4c08727>.

Magnetization measurements; images of the spheroids with maturation days; absorption spectra of the nanosturctures; temperature elevation curves; representative microtomy images; and  $T_2$ -weighted MRI image (PDF)

## ■ AUTHOR INFORMATION

### Corresponding Author

Ali Abou-Hassan – CNRS, Physicochimie des Électrolytes et Nanosystèmes Interfaciaux (PHENIX), Sorbonne Université, F-75005 Paris, France; Institut Universitaire de France (IUF), 75231 Paris, France; [orcid.org/0000-0002-9070-1024](https://orcid.org/0000-0002-9070-1024); Email: [ali.abou\\_hassan@sorbonne-universite.fr](mailto:ali.abou_hassan@sorbonne-universite.fr)

### Authors

Emilia Benassai – CNRS, Physicochimie des Électrolytes et Nanosystèmes Interfaciaux (PHENIX), Sorbonne Université, F-75005 Paris, France

Niéli Daffé – Swiss Light Source, Paul Scherrer Institut, 5232 Villigen, Switzerland; [orcid.org/0000-0002-2225-1658](https://orcid.org/0000-0002-2225-1658)

Elif Aygun – Department of Electrical and Electronics Engineering, Bilkent University, Ankara 06800, Turkey

Audrey Geevding – CNRS, Institut de Biologie Paris-Seine (IBPS), Service de Microscopie Electronique (IBPS-SME),

Sorbonne Université, F-75005 Paris, France; [orcid.org/0000-0002-0208-0302](https://orcid.org/0000-0002-0208-0302)

**Emine Ulku Saritas** – Department of Electrical and Electronics Engineering, Bilkent University, Ankara 06800, Turkey; National Magnetic Resonance Research Center (UMRAM), Bilkent University, Ankara 06800, Turkey

**Claire Wilhelm** – Laboratoire Physico Chimie Curie, Institut Curie, CNRS, PSL Research University, 75006 Paris, France

Complete contact information is available at:  
<https://pubs.acs.org/10.1021/acsami.4c08727>

### Author Contributions

The manuscript was written through contributions of all authors. All authors have given approval to the final version of the manuscript.

### Notes

The authors declare no competing financial interest.

### ACKNOWLEDGMENTS

E.B. and A.A.-H. acknowledge the support of the French Agence Nationale de la Recherche (ANR), under grant ANR-18-CE09-0004 (project MicroNanoCell). A.A.-H. and C.W. acknowledge the support of the French Agence Nationale de la Recherche (ANR), under grant ANR-19-CE09-0029 (project SuperMagStemCells). The authors acknowledge Alexis Canette from the IBPS electron microscopy core facility and the support of Région Île-de-France, Sorbonne-Université, and CNRS for his assistance with sample preparation using the Pelco Biowave instrument. N.D. acknowledges the Swiss National Foundation for the support under the Ambizione grant PZ00P2\_193293. A.A.-H. acknowledges Ana Hortelão for fruitful discussions.

### REFERENCES

- (1) Shieh, D.-B.; Cheng, F.-Y.; Su, C.-H.; Yeh, C.-S.; Wu, M.-T.; Wu, Y.-N.; Tsai, C.-Y.; Wu, C.-L.; Chen, D.-H.; Chou, C.-H. Aqueous dispersions of magnetite nanoparticles with NH<sub>3</sub><sup>+</sup> surfaces for magnetic manipulations of biomolecules and MRI contrast agents. *Biomaterials* **2005**, *26* (34), 7183–7191.
- (2) Rigoni, C.; Fresnais, J.; Talbot, D.; Massart, R.; Perzynski, R.; Bacri, J. C.; Abou-Hassan, A. Magnetic Field-Driven Deformation, Attraction, and Coalescence of Nonmagnetic Aqueous Droplets in an Oil-Based Ferrofluid. *Langmuir* **2020**, *36* (18), 5048–5057.
- (3) Di Corato, R.; Quarta, A.; Piacenza, P.; Ragusa, A.; Figuerola, A.; Buonsanti, R.; Cingolani, R.; Manna, L.; Pellegrino, T. Water solubilization of hydrophobic nanocrystals by means of poly(maleic anhydride-alt-1-octadecene). *J. Mater. Chem.* **2008**, *18* (17), 1991–1996.
- (4) Filippi, M.; Garello, F.; Yasa, O.; Kasamkattil, J.; Scherberich, A.; Katzschmann, R. K. Engineered Magnetic Nanocomposites to Modulate Cellular Function. *Small* **2022**, *18* (9), No. 2104079.
- (5) Van de Walle, A.; Figuerola, A.; Espinosa, A.; Abou-Hassan, A.; Estrader, M.; Wilhelm, C. Emergence of magnetic nanoparticles in photothermal and ferroptotic therapies. *Mater. Horiz.* **2023**, *10* (11), 4757–4775.
- (6) Espinosa, A.; Kolosnjaj-Tabi, J.; Abou-Hassan, A.; Sangnier, A. P.; Curcio, A.; Silva, A. K. A.; Di Corato, R.; Neveu, S.; Pellegrino, T.; Liz-Marzán, L. M.; Wilhelm, C. Magnetic (Hyper)Thermia or Photothermia? Progressive Comparison of Iron Oxide and Gold Nanoparticles Heating in Water, in Cells, and In Vivo. *Adv. Funct. Mater.* **2018**, *28* (37), No. 1803660, DOI: 10.1002/adfm.201803660.
- (7) Gavilán, H.; Avugadda, S. K.; Fernández-Cabada, T.; Soni, N.; Cassani, M.; Mai, B. T.; Chantrell, R.; Pellegrino, T. Magnetic nanoparticles and clusters for magnetic hyperthermia: optimizing their heat performance and developing combinatorial therapies to tackle cancer. *Chem. Soc. Rev.* **2021**, *50*, 11614–11667.
- (8) Avugadda, S. K.; Wickramasinghe, S.; Niculaes, D.; Ju, M.; Lak, A.; Silvestri, N.; Nitti, S.; Roy, I.; Samia, A. C. S.; Pellegrino, T. Uncovering the Magnetic Particle Imaging and Magnetic Resonance Imaging Features of Iron Oxide Nanocube Clusters. *Nanomaterials* **2021**, *11* (1), No. 62, DOI: 10.3390/nano11010062.
- (9) Cazares-Cortes, E.; Cabana, S.; Boitard, C.; Nehlig, E.; Griffete, N.; Fresnais, J.; Wilhelm, C.; Abou-Hassan, A.; Ménager, C. Recent insights in magnetic hyperthermia: From the “hot-spot” effect for local delivery to combined magneto-photo-thermia using magneto-plasmonic hybrids. *Adv. Drug Delivery Rev.* **2019**, *138*, 233–246.
- (10) Jain, T. K.; Reddy, M. K.; Morales, M. A.; Leslie-Pelecky, D. L.; Labhasetwar, V. Biodistribution, Clearance, and Biocompatibility of Iron Oxide Magnetic Nanoparticles in Rats. *Mol. Pharmaceutics* **2008**, *5* (2), 316–327.
- (11) Nemeč, S.; Kralj, S.; Wilhelm, C.; Abou-Hassan, A.; Rols, M.-P.; Kolosnjaj-Tabi, J. Comparison of iron oxide nanoparticles in photothermia and magnetic hyperthermia: Effects of clustering and silica encapsulation on nanoparticles’ heating yield. *Appl. Sci.* **2020**, *10* (20), No. 7322, DOI: 10.3390/app10207322.
- (12) Cabana, S.; Curcio, A.; Michel, A.; Wilhelm, C.; Abou-Hassan, A. Iron oxide mediated photothermal therapy in the second biological window: A comparative study between magnetite/maghemite nanospheres and nanoflowers. *Nanomaterials* **2020**, *10* (8), No. 1548, DOI: 10.3390/nano10081548.
- (13) Roca, A. G.; Lopez-Barbera, J. F.; Lafuente, A.; Özel, F.; Fantechi, E.; Muro-Cruces, J.; Hémadi, M.; Sepulveda, B.; Noguees, J. Iron oxide nanoparticles (Fe<sub>3</sub>O<sub>4</sub>,  $\gamma$ -Fe<sub>2</sub>O<sub>3</sub> and FeO) as photothermal heat mediators in the first, second and third biological windows. *Phys. Rep.* **2023**, *1043*, 1–35.
- (14) Bertuit, E.; Benassai, E.; Méridet, G.; Greneche, J.-M.; Baptiste, B.; Neveu, S.; Wilhelm, C.; Abou-Hassan, A. Structure–Property–Function Relationships of Iron Oxide Multicore Nanoflowers in Magnetic Hyperthermia and Photothermia. *ACS Nano* **2022**, *16* (1), 271–284.
- (15) Bertuit, E.; Menguy, N.; Wilhelm, C.; Rollet, A.-L.; Abou-Hassan, A. Angular orientation between the cores of iron oxide nanoclusters controls their magneto–optical properties and magnetic heating functions. *Commun. Chem.* **2022**, *5* (1), No. 164, DOI: 10.1038/s42004-022-00787-0.
- (16) Gallo-Cordova, A.; Ovejero, J. G.; Pablo-Sainz-Ezquerro, A. M.; Cuya, J.; Jeyadevan, B.; Veintemillas-Verdaguer, S.; Tartaj, P.; del Puerto Morales, M. Unravelling an amine-regulated crystallization crossover to prove single/multicore effects on the biomedical and environmental catalytic activity of magnetic iron oxide colloids. *J. Colloid Interface Sci.* **2022**, *608*, 1585–1597.
- (17) Gavilán, H.; Sánchez, E. H.; Brollo, M. E. F.; Asín, L.; Moerner, K. K.; Frandsen, C.; Lázaro, F. J.; Serna, C. J.; Veintemillas-Verdaguer, S.; Morales, M. P.; Gutiérrez, L. Formation Mechanism of Maghemite Nanoflowers Synthesized by a Polyol-Mediated Process. *ACS Omega* **2017**, *2* (10), 7172–7184.
- (18) Hemery, G.; Keyes, A. C.; Garaio, E.; Rodrigo, I.; Garcia, J. A.; Plazaola, F.; Garanger, E.; Sandre, O. Tuning Sizes, Morphologies, and Magnetic Properties of Monocore Versus Multicore Iron Oxide Nanoparticles through the Controlled Addition of Water in the Polyol Synthesis. *Inorg. Chem.* **2017**, *56* (14), 8232–8243.
- (19) Roy, S.; Liu, Z.; Sun, X.; Gharib, M.; Yan, H.; Huang, Y.; Megahed, S.; Schnabel, M.; Zhu, D.; Feliu, N.; et al. Assembly and Degradation of Inorganic Nanoparticles in Biological Environments. *Bioconjugate Chem.* **2019**, *30* (11), 2751–2762.
- (20) Feliu, N.; Docter, D.; Heine, M.; del Pino, P.; Ashraf, S.; Kolosnjaj-Tabi, J.; Macchiarini, P.; Nielsen, P.; Alloyeau, D.; Gazeau, F.; et al. In vivo degeneration and the fate of inorganic nanoparticles. *Chem. Soc. Rev.* **2016**, *45* (9), 2440–2457.
- (21) Lu, H.; Stenzel, M. H. Multicellular Tumor Spheroids (MCTS) as a 3D In Vitro Evaluation Tool of Nanoparticles. *Small* **2018**, *14* (13), No. 1702858.

- (22) Curcio, A.; de Walle, A. V.; Benassai, E.; Serrano, A.; Luciani, N.; Menguy, N.; Manshian, B. B.; Sargsian, A.; Soenen, S.; Espinosa, A.; et al. Massive intracellular remodeling of CuS nanomaterials produces nontoxic bioengineered structures with preserved photothermal potential. *ACS Nano* **2021**, *15* (6), 9782–9795.
- (23) Mazuel, F.; Espinosa, A.; Radtke, G.; Bugnet, M.; Neveu, S.; Lalatonne, Y.; Botton, G. A.; Abou-Hassan, A.; Wilhelm, C. Magneto-thermal metrics can mirror the long-term intracellular fate of magneto-plasmonic nanohybrids and reveal the remarkable shielding effect of gold. *Adv. Funct. Mater.* **2017**, *27* (9), No. 1605997.
- (24) Espinosa, A.; Curcio, A.; Cabana, S.; Radtke, G.; Bugnet, M.; Kolosnjaj-Tabi, J.; P echoux, C.; Alvarez-Lorenzo, C.; Botton, G. A.; Silva, A. K. A.; et al. Intracellular Biodegradation of Ag Nanoparticles, Storage in Ferritin, and Protection by a Au Shell for Enhanced Photothermal Therapy. *ACS Nano* **2018**, *12* (7), 6523–6535.
- (25) Zhu, L.; Pelaz, B.; Chakraborty, I.; Parak, W. J. Investigating Possible Enzymatic Degradation on Polymer Shells around Inorganic Nanoparticles. *Int. J. Mol. Sci.* **2019**, *20* (4), No. 935, DOI: 10.3390/ijms20040935.
- (26) Fern andez-Afonso, Y.; As n, L.; Beola, L.; Fratila, R. M.; Guti errez, L. Influence of Magnetic Nanoparticle Degradation in the Frame of Magnetic Hyperthermia and Photothermal Treatments. *ACS Appl. Nano Mater.* **2022**, *5* (11), 16220–16230.
- (27) Sangnier, A. P.; Van de Walle, A. B.; Curcio, A.; Le Borgne, R.; Motte, L.; Lalatonne, Y.; Wilhelm, C. Impact of magnetic nanoparticle surface coating on their long-term intracellular biodegradation in stem cells. *Nanoscale* **2019**, *11* (35), 16488–16498, DOI: 10.1039/C9NR05624F.
- (28) Portilla, Y.; Fern andez-Afonso, Y.; P erez-Yag ue, S.; Mulens-Arias, V.; Morales, M. P.; Guti errez, L.; Barber, D. F. Different coatings on magnetic nanoparticles dictate their degradation kinetics in vivo for 15 months after intravenous administration in mice. *J. Nanobiotechnol.* **2022**, *20* (1), No. 543, DOI: 10.1186/s12951-022-01747-5.
- (29) Kr etowski, R.; Kusaczuk, M.; Naumowicz, M.; Koty nska, J.; Szynaka, B.; Cechowska-Pasko, M. The Effects of Silica Nanoparticles on Apoptosis and Autophagy of Glioblastoma Cell Lines. *Nanomaterials* **2017**, *7* (8), No. 230, DOI: 10.3390/nano7080230.
- (30) Boitard, C.; Curcio, A.; Rollet, A.-L.; Wilhelm, C.; M enager, C.; Griffete, N. Biological Fate of Magnetic Protein-Specific Molecularly Imprinted Polymers: Toxicity and Degradation. *ACS Appl. Mater. Interfaces* **2019**, *11* (39), 35556–35565.
- (31) Habault, D.; Dery, A.; Leng, J.; Lecommandoux, S.; Meins, J. F. L.; Sandre, O. Droplet Microfluidics to Prepare Magnetic Polymer Vesicles and to Confine the Heat in Magnetic Hyperthermia. *IEEE Trans. Magn.* **2013**, *49* (1), 182–190.
- (32) Robb, M. J.; Connal, L. A.; Lee, B. F.; Lynd, N. A.; Hawker, C. J. Functional block copolymer nanoparticles: toward the next generation of delivery vehicles. *Polym. Chem.* **2012**, *3* (6), 1618–1628.
- (33) Lecommandoux, S.; Sandre, O.; Ch ecot, F.; Rodriguez-Hernandez, J.; Perzynski, R. Self-assemblies of magnetic nanoparticles and di-block copolymers: Magnetic micelles and vesicles. *J. Magn. Mater.* **2006**, *300* (1), 71–74.
- (34) Berret, J.-F.; Schonbeck, N.; Gazeau, F.; El Kharrat, D.; Sandre, O.; Vacher, A.; Airiau, M. Controlled Clustering of Superparamagnetic Nanoparticles Using Block Copolymers: Design of New Contrast Agents for Magnetic Resonance Imaging. *J. Am. Chem. Soc.* **2006**, *128* (5), 1755–1761.
- (35) Hickey, R. J.; Haynes, A. S.; Kikkawa, J. M.; Park, S.-J. Controlling the Self-Assembly Structure of Magnetic Nanoparticles and Amphiphilic Block-Copolymers: From Micelles to Vesicles. *J. Am. Chem. Soc.* **2011**, *133* (5), 1517–1525.
- (36) Mai, Y.; Eisenberg, A. Self-assembly of block copolymers. *Chem. Soc. Rev.* **2012**, *41* (18), 5969–5985.
- (37) Vilsinski, B. H.; Witt, M. A.; Barbosa, P. M.; Montanha, M. C.; Nunes, C. S.; Bellettini, I. C.; de Castro, L. V.; Sato, F.; Baesso, M. L.; Muniz, E. C.; Caetano, W. Formulation of chloroaluminum phthalocyanine incorporated into PS-b-PAA diblock copolymer nanomicelles. *J. Mol. Liq.* **2018**, *271*, 949–958.
- (38) Vyh nalkova, R.; Eisenberg, A.; van de Ven, T. G. M. Loading and Release Mechanisms of a Biocide in Polystyrene-Block-Poly(acrylic acid) Block Copolymer Micelles. *J. Phys. Chem. B* **2008**, *112* (29), 8477–8485.
- (39) Benassai, E.; Hortelao, A. C.; Aygun, E.; Alpman, A.; Wilhelm, C.; Saritas, E. U.; Abou-Hassan, A. High-throughput large scale microfluidic assembly of iron oxide nanoflowers@PS-b-PAA polymeric micelles as multimodal nanoplatforms for photothermia and magnetic imaging. *Nanoscale Adv.* **2023**, *6* (1), 126–135.
- (40) del Monte, F.; Morales, M. P.; Levy, D.; Fernandez, A.; Oca na, M.; Roig, A.; Molins, E.; O’Grady, K.; Serna, C. J. Formation of  $\gamma$ -Fe<sub>2</sub>O<sub>3</sub> Isolated Nanoparticles in a Silica Matrix. *Langmuir* **1997**, *13* (14), 3627–3634.
- (41) Haddad, P. S.; Duarte, E. L.; Baptista, M. S.; Goya, G. F.; Leite, C. A.; Itri, R. Synthesis and Characterization of Silica-Coated Magnetic Nanoparticles. In *Surface and Colloid Science*, Progress in Colloid and Polymer Science; Springer, 2004; pp 232–238.
- (42) Lojk, J.; Bregar, V. B.; Rajh, M.; Mi , K.; Kreft, M. E.; Pirkmajer, S.; Verani , P.; Pavlin, M. Cell type-specific response to high intracellular loading of polyacrylic acid-coated magnetic nanoparticles. *Int. J. Nanomed.* **2015**, *10*, 1449–1462.
- (43) Wahsner, J.; Gale, E. M.; Rodr guez-Rodr guez, A.; Caravan, P. Chemistry of MRI Contrast Agents: Current Challenges and New Frontiers. *Chem. Rev.* **2019**, *119* (2), 957–1057.
- (44) Eichhorn, J.; Gordievskaya, Y. D.; Kramarenko, E. Y.; Khokhlov, A. R.; Schacher, F. H. pH-Dependent Structure of Block Copolymer Micelles Featuring a Polyampholyte Corona: A Combined Experimental and Theoretical Approach. *Macromolecules* **2021**, *54* (4), 1976–1991.
- (45) Kuiper, P.; Searle, B. G.; Duda, L. C.; Wolf, R. M.; van der Zaag, P. J. Fe L<sub>2,3</sub> linear and circular magnetic dichroism of Fe<sub>3</sub>O<sub>4</sub>. *J. Electron Spectrosc. Relat. Phenom.* **1997**, *86* (1), 107–113.
- (46) Carvallo, C.; Sainctavit, P.; Arrio, M.-A.; Menguy, N.; Wang, Y.; Ona-Nguema, G.; Brice-Profeta, S. Biogenic vs. abiogenic magnetite nanoparticles: A XMCD study. *Am. Mineral.* **2008**, *93* (5–6), 880–885.
- (47) Lee, Y.; Lee, J.; Bae, C. J.; Park, J.-G.; Noh, H.-J.; Park, J.-H.; Hyeon, T. Large-Scale Synthesis of Uniform and Crystalline Magnetite Nanoparticles Using Reverse Micelles as Nanoreactors under Reflux Conditions. *Adv. Funct. Mater.* **2005**, *15* (3), 503–509.
- (48) Gilbert, B.; Katz, J. E.; Denlinger, J. D.; Yin, Y.; Falcone, R.; Waychunas, G. A. Soft X-ray Spectroscopy Study of the Electronic Structure of Oxidized and Partially Oxidized Magnetite Nanoparticles. *J. Phys. Chem. C* **2010**, *114* (50), 21994–22001.
- (49) Coker, V. S.; Pearce, C. I.; Lang, C.; van der Laan, G.; Patrick, R. A. D.; Telling, N. D.; Sch uler, D.; Arenholz, E.; Lloyd, J. R. Cation site occupancy of biogenic magnetite compared to polygenic ferrite spinels determined by X-ray magnetic circular dichroism. *Eur. J. Mineral.* **2007**, *19* (5), 707–716.
- (50) Guyodo, Y.; Sainctavit, P.; Arrio, M.-A.; Carvallo, C.; Penn, R. L.; Erbs, J. J.; Forsberg, B. S.; Morin, G.; Maillot, F.; Lagroix, F. et al. X-ray magnetic circular dichroism provides strong evidence for tetrahedral iron in ferrihydrite. *Geochem., Geophys., Geosyst.* **2012**; Vol. 13 6 DOI: 10.1029/2012GC004182.
- (51) Everett, J.; Brooks, J.; Lermite, F.; O’Connor, P. B.; Sadler, P. J.; Dobson, J.; Collingwood, J. F.; Telling, N. D. Iron stored in ferritin is chemically reduced in the presence of aggregating  $\alpha\beta$ (1–42). *Sci. Rep.* **2020**, *10* (1), No. 10332.